Progress In Electromagnetics Research, PIER 81, 21–39, 2008

VECTOR FINITE ELEMENT ANALYSIS OF MULTICOMPONENT INDUCTION RESPONSE IN ANISOTROPIC FORMATIONS

X. Y. Sun and Z. P. Nie

School of Electronic Engineering
University of Electronic Science and Technology of China
Chengdu 610054, China

Abstract—Multicomponent induction logging responses are simulated by using hierarchical mixed order vector finite element method (FEM). In order to modeling three orthogonal magnetic dipoles, we adopt the method that the total field is separated into incident field and secondary field, and only the secondary field is computed by FEM. In addition, two techniques are applied to improve the modeling accuracy and computational efficiency: 1) Hierarchical mixed order vector basis functions are applied to FEM. Different order basis functions are used in different elements in accordance with the changing speed of the field. The mixed order scheme reduces greatly the number of unknowns without reducing accuracy, and can attain much higher computational efficiency. 2) The system of the FEM equations is solved by Distributed-SuperLU, and the results of multiple measure points can be got simultaneously. The FEM result is validated against volume integral equation method and the approach of planar layered media Green's functions, and the comparisons show very good agreement. Finally, the multicomponent induction response in anisotropic formations involving eccentric tools and dipping beds is included to demonstrate the flexibility of the method.

1. INTRODUCTION

Conventional induction logging tools comprising the axial direction component of transmitter and receiver can only provide coaxial measurements, which only yield horizontal resistivity for a vertical well or some weighted value of vertical resistivity and horizontal resistivity for a deviated or horizontal well. However, for thinly laminated sand and shale reservoir rocks, whose individual beds are beyond the resolution limits of conventional induction tools, the macro-resistivity is anisotropic, and a multicomponent electromagnetic induction logging tool has been developed to try to simultaneously evaluate the horizontal and vertical resistivity of the earth formations [1, 15]. In addition to the coaxial transmitter-receiver pair, the new tool has two mutually orthogonal coplanar transmitter-receiver pairs, so theoretically it can provide nine components of magnetic field produced by the three mutually orthogonal transmitters. Therefore, the multicomponent electromagnetic induction measurement can resolve the anisotropic resistivity of earth formations.

Since the model of multicomponent induction logging tools in borehole environment is completely three dimensional, the system cannot be solved by fast algorithms such as numerical mode matching method [22]; rather, three dimensional numerical methods such as finite difference [21], finite difference time domain [17–20], finite element [23, 24] and integral Equation [25–28] have to be employed. In general, finite difference methods are employed [2, 3] for three-dimensional numerical modeling of the new tools. The author employs the vector finite element method to simulate multi-component induction logging tools. The separation of the total electric field into incident and secondary field makes it possible that the technique proposed is suitable for the magnetic dipole in any direction and for the tool eccentricity problem. 3-D cylindrical grids are used to avoid staircase discretization errors in borehole geometries. We implement the FEM with hierarchical mixed order vector basis functions to improve the computational efficiency. The field varies greatly in the region near the source [16], thus by using higher order basis functions, we can easily model these complex changes; however, the field varies slowly in the farther region, thus it will be sufficient to use the lowest order basis functions. The number of unknowns could be greatly reduced if we apply basis functions of different orders to different regions. Then the linear equations are solved by Distributed SuperLU, and we can get the simulation results of multiple measure points by decomposing the matrix only once. Finally, we validate the FEM results against both the volume integral equation method and the approach of planar layered media Green's functions, and illustrate the application of the algorithm in several different borehole problems.

2. THEORIES

2.1. The Variational Formulation

For an inhomogeneous anisotropic medium, Maxwell equation with a magnetic current density $\boldsymbol{M}$ can be written as:

$$\nabla\times\boldsymbol{E} = -j\omega\mu\boldsymbol{H}-\boldsymbol{M} \tag{1}$$

$$\nabla\times\boldsymbol{H} = j\omega\varepsilon_0\bar{\varepsilon}_r\cdot\boldsymbol{E} \tag{2}$$

where $\bar{\varepsilon}_r$ is the complex relative permittivity tensor

$$\bar{\varepsilon}_r=\frac{1}{\varepsilon_0}(\varepsilon\bar{\boldsymbol{I}}-j\bar{\sigma}/\omega) \tag{3}$$

where $\bar{\boldsymbol{I}}$ is the unit tensor. If we suppose that the conductivity of the formation is uniaxially anisotropic, then $\bar{\sigma}$ can be expressed as:

$$\bar{\sigma}=\begin{bmatrix}\sigma_H & & \\ & \sigma_H & \\ & & \sigma_V\end{bmatrix} \tag{4}$$

where $\sigma_{H,V}$ is the horizontal and vertical conductivity respectively. From Equation (1) we get the wave equation:

$$\nabla\times\left(\frac{1}{\mu_r}\nabla\times\boldsymbol{E}\right)-k_0^2\bar{\varepsilon}_r\cdot\boldsymbol{E}=-\nabla\times\left(\frac{1}{\mu_r}\boldsymbol{M}\right) \tag{5}$$

where μ_r is the relative permeability, $k_0=\omega^2\varepsilon_0u_0$. We then decompose the total field into incident and secondary field.

$$\boldsymbol{E}=\boldsymbol{E}^i+\boldsymbol{E}^s \tag{6}$$

where $\boldsymbol{E}^i$ is the incident field produced by a magnetic current $\boldsymbol{M}$ in a homogeneous isotropic background medium. The incident field satisfies the wave equation:

$$\nabla\times\left(\frac{1}{\mu_r}\nabla\times\boldsymbol{E}^i\right)-k_0^2\varepsilon_b\boldsymbol{E}^i=-\nabla\times\left(\frac{1}{\mu_r}\boldsymbol{M}\right) \tag{7}$$

where ε_b is the relative permittivity of background medium. After substituting (5) into (4) minus (6), we have:

$$\nabla\times\left(\frac{1}{\mu_r}\nabla\times\boldsymbol{E}^s\right)-k_0^2\bar{\varepsilon}_r\boldsymbol{E}^s=k_0\left(\bar{\varepsilon}_r-\varepsilon_b\bar{\boldsymbol{I}}\right)\boldsymbol{E}^i \tag{8}$$

In general, the solution domain is truncated by the outer surface at the position where the field is small enough. In this paper, the outer truncation surface is around 3.5 times the skin depth away from the transmitter. On the outer truncation surface, the Equation (7) is subject to boundary conditions:

$$\hat{\boldsymbol{n}} \times \boldsymbol{E} = 0 \tag{9}$$

In accordance with the variational principle [4], the secondary field governed by Equation (7) can be obtained by seeking the stationary point of the functional:

$$\begin{aligned} F(\boldsymbol{E}^s) \; = \; & \frac{1}{2} \iiint_V \left[\frac{1}{\mu_r} (\nabla \times \boldsymbol{E}^s) \cdot (\nabla \times \boldsymbol{E}^s) - k_0^2 \boldsymbol{E}^s \cdot \bar{\varepsilon}_r \cdot \boldsymbol{E}^s \right] dV \\ & - k_0^2 \iiint_V \boldsymbol{E}^s \cdot \left(\bar{\varepsilon}_r - \varepsilon_b \bar{\boldsymbol{I}} \right) \cdot \boldsymbol{E}^i dV \end{aligned} \tag{10}$$

If the magnetic dipole in the axial direction is located at the origin, this incident electric field in Equation (9) can be expressed in the cylindrical coordinate as [5]:

$$\boldsymbol{E}^i = \hat{\boldsymbol{\varphi}} \frac{M}{4\pi} \frac{\rho e^{i k_b \boldsymbol{r}}}{\boldsymbol{r}^3} (1 - i k_b \boldsymbol{r}) \tag{11}$$

where $M (M = i\omega u_b I S_0)$ is the magnetic moment of the dipole; S_0 is the area enclosed by the coil; $\rho = \sqrt{x^2 + y^2}$; $k_b = \omega^2 \varepsilon_b u$. As for the incident field produced by magnetic dipole in other directions, we can easily get them by multiplying the Equation (10) by a rotation matrix as a result of the rotation of the coordinate.

2.2. Domain Discretization

First, we must discretize the solution domain Ω. In finite element analysis of induction logging, the tetrahedral grids or rectangular brick grids are usually used for discretization [7, 8], while in this article, hexahedral grids in cylindrical coordinate is used instead. The mesh illustration is shown in Fig. 1, from which we can see that cylindrical hexahedral grids can automatically conform to borehole wall and can avoid staircase error. Besides, the cell size is uniform in the azimuthal ϕ direction and in the longitudinal z direction of the measure domain, while the cell size is nonuniform in the radial ρ direction and in longitudinal z direction of the domain outside the measure domain, and $\Delta\rho$ and Δz is gradually increased to minimize the number of mesh grids and unknowns required.

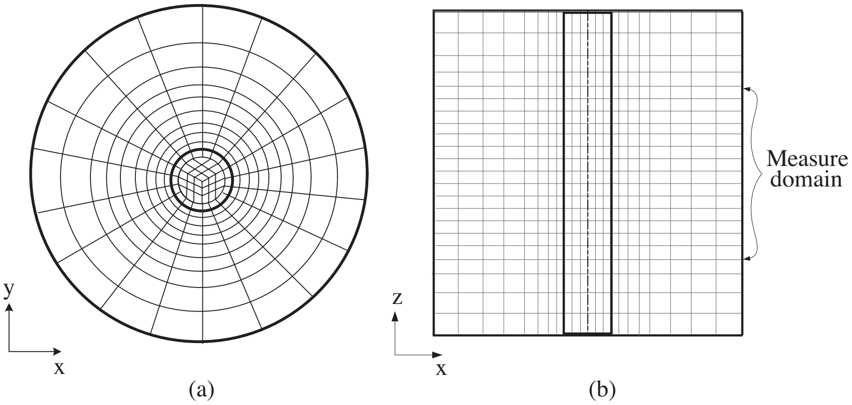

Figure 1. Illustration of the mesh with (a) a $z = 0$ slice in the horizontal x/y-plane and (b) a $y = 0$ slice in the vertical x/z-plane through a hexahedral mesh.

2.3. Hierarchical Mixed Order Vector Basis Functions

A hexahedral element in xyz-Cartesian coordinate system can be transformed into the cubic element in the new uvw-coordinate system, as shown in Fig. 2. The required transformation can be expressed as:

$$\boldsymbol{r}(u, v, w) = \sum_{i=1}^{8} N_i^e(u, v, w)\boldsymbol{r}_i \tag{12}$$

where $\boldsymbol{r}_i$ is the position vector of the ith node in xyz coordinate system and

$$N_i(u, v, w) = \frac{1}{8}(1 + u_i u)(1 + v_i v)(1 + w_i w) \quad -1 \leq u, v, w \leq 1 \tag{13}$$

with (u_i, v_i, w_i) denoting the coordinate value of the ith node in uvw coordinate system.

The electric field in every hexahedron can be represented as

$$\begin{aligned}\boldsymbol{E}^s \;=\; & \sum_{i=0}^{N_u-1}\sum_{j=0}^{N_v}\sum_{k=0}^{N_w}\alpha_{uijk}\boldsymbol{f}_{uijk} + \sum_{i=0}^{N_u}\sum_{j=0}^{N_v-1}\sum_{k=0}^{N_w}\alpha_{vijk}\boldsymbol{f}_{vijk} \\ & + \sum_{i=0}^{N_u}\sum_{j=0}^{N_v}\sum_{k=0}^{N_w-1}\alpha_{wijk}\boldsymbol{f}_{wijk}\end{aligned} \tag{14}$$

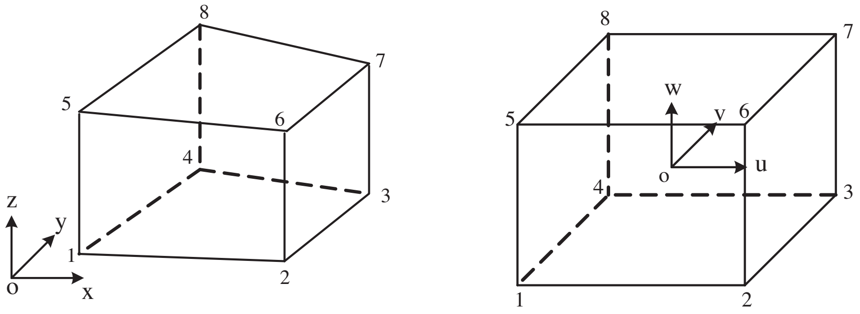

(a) (b)

Figure 2. (a) Hexahedral element in the xyz-coordinate system. (b) Cubic element in the uvw-coordinate system after transformation.

where $\boldsymbol{f}$ are hierarchical-type vector basis functions [6] defined as

$$\begin{aligned} \boldsymbol{f}_{uijk} &= u^i P_j(v) P_k(w) \boldsymbol{a}_u \\ \boldsymbol{f}_{vijk} &= P_i(u) v^j P_k(w) \boldsymbol{a}_v \\ \boldsymbol{f}_{wijk} &= P_i(u) P_j(v) w^k \boldsymbol{a}_w \\ P_n(u) &= \begin{cases} 1-u & n=0 \\ 1+u & n=1 \\ u^n-1 & n\geq 2,\ \text{even} \\ u^n-u & n\geq 2,\ \text{odd} \end{cases} \end{aligned} \tag{15}$$

Sum limits N_u, N_v,and N_w are the adopted degrees of the polynomial approximation and α_{uijk}, α_{vijk}, and α_{wijk} are unknown coefficients. The reciprocal unitary vectors $\boldsymbol{a}_u$, $\boldsymbol{a}_v$, $\boldsymbol{a}_w$ are defined as

$$\boldsymbol{a}_u = \frac{1}{J}\left(\frac{d\boldsymbol{r}}{dv}\times\frac{d\boldsymbol{r}}{dw}\right),\ \ \boldsymbol{a}_v = \frac{1}{J}\left(\frac{d\boldsymbol{r}}{dw}\times\frac{d\boldsymbol{r}}{du}\right),\ \ \boldsymbol{a}_v = \frac{1}{J}\left(\frac{d\boldsymbol{r}}{du}\times\frac{d\boldsymbol{r}}{dv}\right) \tag{16}$$

where J is Jacobian of covariant transformation

$$J = \left(\frac{d\boldsymbol{r}}{du}\times\frac{d\boldsymbol{r}}{dv}\right)\cdot\frac{d\boldsymbol{r}}{dw} \tag{17}$$

As for induction problems, the field has an acute variation near the transmitter and higher order basis functions $N_u > 1$ or $N_v > 1$ or $N_w > 1$ are used to expand it in the shadow region shown in Fig. 3. (The shadow region refers to the nearby region passed through by the multicomponent tool.) The field varies slowly in farther region and we adopt the lowest (one) order basis functions $N_u = 1$, $N_v = 1$, and

$N_w = 1$ for the non-shadow region, as shown in Fig. 3. Field expansion using lowest and higher order selectively is very attractive to the simulation of induction problem. In the shadow region where we expect great field variation, fewer unknowns are sufficient to describe precisely the acutely changing fields because of higher order basis functions; in the non-shadow region where we expect slight field variation, the lowest order is sufficient to describe it. In this way, we can reduce the number of unknowns and still have an adequately accurate solution.

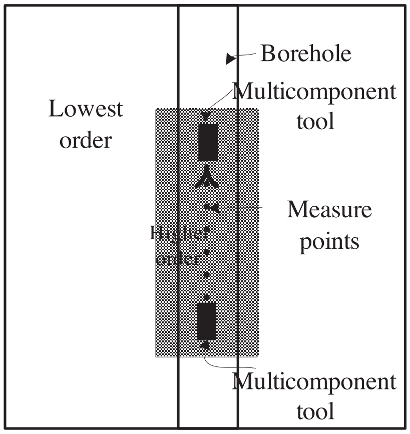

Figure 3. Illustration of the distribution of different order basis functions.

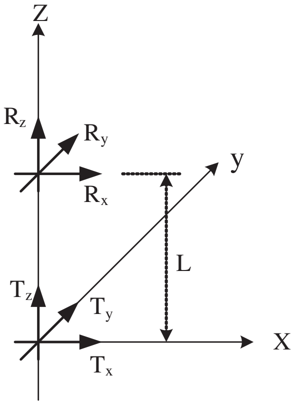

Figure 4. Illustration of the basic structure of multicomponent induction logging tool.

2.4. Finite Element Analysis

We discretize the function defined in (9), and represent it with an integral sum of all elements expressed by "e".

$$\begin{aligned} F(\boldsymbol{E}^s) &= \sum_{e=1}^{M} F_e(\boldsymbol{E}^s) \\ &= \frac{1}{2}\sum_{e=1}^{M}\iiint_{V^e}\left[\frac{1}{\mu_r}(\nabla\times\boldsymbol{E}^s)\cdot(\nabla\times\boldsymbol{E}^s) - k_0^2\boldsymbol{E}^s\cdot\bar{\varepsilon}_r\cdot\boldsymbol{E}^s\right]dV \\ &\quad -k_0^2\sum_{e=1}^{M}\iiint_{V}\boldsymbol{E}^s\cdot\left(\bar{\varepsilon}_r-\varepsilon_b\bar{\boldsymbol{I}}\right)\cdot\boldsymbol{E}^i dV \qquad (18) \end{aligned}$$

where M is the total number of elements. Within each element, the curl of the secondary field $\boldsymbol{E}^s$ can be expressed as

$$\begin{aligned}\nabla\times\boldsymbol{E}^s \;=\;& \sum_{i=0}^{N_u-1}\sum_{j=0}^{N_v}\sum_{k=0}^{N_w}\alpha_{uijk}\nabla\times\boldsymbol{f}_{uijk}+\sum_{i=0}^{N_u}\sum_{j=0}^{N_v-1}\sum_{k=0}^{N_w}\alpha_{vijk}\nabla\times\boldsymbol{f}_{vijk}\\ &+\sum_{i=0}^{N_u}\sum_{j=0}^{N_v}\sum_{k=0}^{N_w-1}\alpha_{wijk}\nabla\times\boldsymbol{f}_{wijk} \qquad (19)\end{aligned}$$

where the curl of $\boldsymbol{f}$ can be computed by [6]

$$\begin{aligned}\nabla\times\boldsymbol{f}_{uijk} &= \frac{1}{J}\left[u^iP_j(v)\frac{dP_k(w)}{dw}\frac{d\boldsymbol{r}}{dv}-u^i\frac{dP_j(v)}{dv}P_k(w)\frac{d\boldsymbol{r}}{dw}\right]\\ \nabla\times\boldsymbol{f}_{vijk} &= \frac{1}{J}\left[v^jP_k(w)\frac{dP_i(u)}{du}\frac{d\boldsymbol{r}}{dw}-v^j\frac{dP_k(w)}{dw}P_i(u)\frac{d\boldsymbol{r}}{du}\right] \qquad (20)\\ \nabla\times\boldsymbol{f}_{wijk} &= \frac{1}{J}\left[w^iP_i(u)\frac{dP_j(v)}{dv}\frac{d\boldsymbol{r}}{du}-u^k\frac{dP_i(u)}{du}P_j(v)\frac{d\boldsymbol{r}}{dv}\right]\end{aligned}$$

Substituting (13) and (18) into (17), one obtains

$$F(\boldsymbol{E}^s)=\frac{1}{2}\sum_{e=1}^{M}\{\alpha^e\}^T\left[\boldsymbol{K}^e\right]\{\alpha^e\}-\sum_{e=1}^{M}\{\alpha^e\}^T\{b^e\} \qquad (21)$$

where the elemental matrix and vector are given by

$$\begin{aligned}[\boldsymbol{K}^e] &= \iiint\limits_{V^e}\left[\frac{1}{\mu_r^e}\{\nabla\times\boldsymbol{f}^e\}\cdot\{\nabla\times\boldsymbol{f}^e\}^T-k_0^2\{\boldsymbol{f}^e\}\cdot\bar{\bar{\varepsilon}}_r^e\cdot\{\boldsymbol{f}^e\}^T\right]dV \qquad (22)\\ \{b^e\} &= -k_0^2\iiint\limits_{V^e}\left[\{\boldsymbol{f}^e\}\cdot\left(\bar{\bar{\varepsilon}}_r^e-\bar{\boldsymbol{I}}\varepsilon_b\right)\cdot\boldsymbol{E}^i\right]dV \qquad (23)\end{aligned}$$

After taking the partial derivative of F with respect to α^e, we can impose the stationarity requirement on F to find the system of equations

$$[\boldsymbol{K}]\{\alpha\}=\{b\} \qquad (24)$$

where

$$[\boldsymbol{K}]=\sum_{e=1}^{M}[\boldsymbol{K}^e],\quad \{b\}=\sum_{e=1}^{M}\{b^e\} \qquad (25)$$

2.5. Solution of Finite Element Equations

In general, the linear Equation (23) are solved by iteration method. Because of the large condition numbers of matrix $[\boldsymbol{K}]$, the convergence rate of iteration solution is very slow. Besides, whenever one measure point is changed, although the matrix $[\boldsymbol{K}]$ remains the same, we need a new iteration solution due to the change of vector $\{b\}$. If LU decomposition of $[\boldsymbol{K}]$ is used, we can get multiple measure point values by decomposition of only once.

Over the years, the LU decomposition has been significantly improved for sparse matrix equations [9, 10]. A newly developed package, Distributed SuperLU [11], is incorporated into our implementation of the FEM algorithm for LU decomposition and the solution of linear equations.

3. NUMERICAL RESULTS

In this section, several numerical examples are employed to verify the FEM algorithm and illustrate the applications of the FEM algorithm in simulation of multi-component induction logging tools. In addition, we compare the computational time and accuracy of field using one order and mixed order basis functions respectively. The basic structure of multi-component induction tool is showed in Fig. 4. T_x, T_y and T_z are the three mutually orthogonal transmitter coils; R_x, R_y and R_z are the three mutually orthogonal receiver coils. The parameters used for the computation of the following examples, except for special reference, are as follows: The frequency of operation is 20 kHz; the distance between the transmitter and receiver is $L = 0.8\,\text{m}$; the three apparent conductivities are computed by the following formulae [12].

$$\sigma_{xx}^a = \frac{8\pi L}{\mu}\text{Im}(H_{xx}), \quad \sigma_{yy}^a = \frac{8\pi L}{\mu}\text{Im}(H_{yy}), \quad \sigma_{zz}^a = \frac{4\pi L}{\mu}\text{Im}(H_{zz}) \tag{26}$$

where σ_{xx}^a and σ_{yy}^a are called the apparent vertical conductivities, and σ_{zz}^a is called the horizontal conductivity.

To validate our FEM algorithm and program, we first compare the FEM results for three-layered anisotropic formation with the analytic results computed by the multilayered media Green's functions [13]. The formation's vertical conductivity σ_v and horizontal conductivity σ_h are shown as the dot line and dash dot line respectively in Fig. 5. We compute the apparent horizontal conductivity and apparent vertical conductivity by the two methods, and Fig. 5 shows excellent agreement between FEM results and analytic results.

Another comparison of our results with an independently derived solution by Avdeev [14] is presented in Fig. 6(b). The computed model

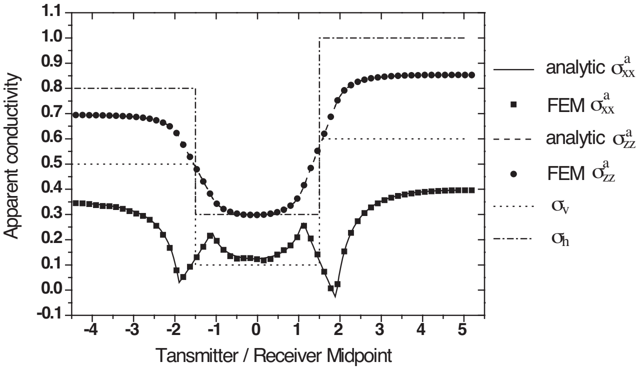

Figure 5. Response of three-layered anisotropic formations computed by FEM and multilayered media Green's functions.

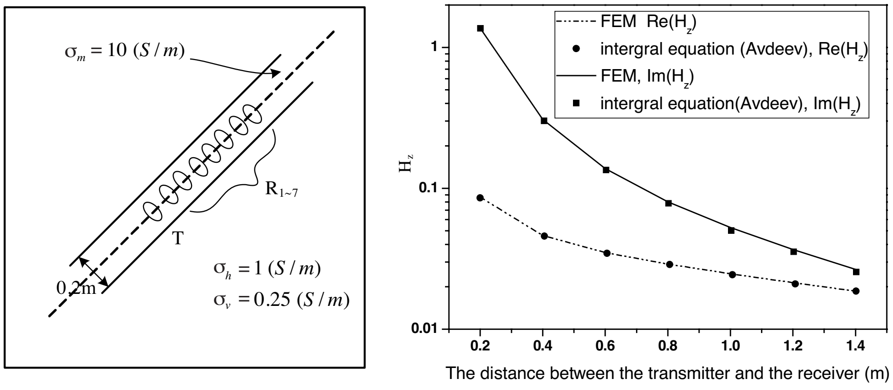

(a) (b)

Figure 6. Comparison of the FEM results for axial magnetic field with the results of integral equation.

is shown in Fig. 6(a) with an axial 160-kHz transmitter and several receiver coils along the axis of a conductive borehole intersecting a dipping anisotropic formation. One can see that the real part and imaginary part of the magnetic field are very close to those computed by integral equation method by Avdeev.

Then, to compare the computational efficiency and accuracy using one order basis functions and mixed order basis functions respectively, we simulate the two-layered formation, as shown in Fig. 7(a), in which the shadow region refers to the nearby domain passed through by the multicomponent tool. We employ the two methods with different basis functions to compute the model. First, one order basis functions ($N_u = 1,\ N_v = 1,\ N_w = 1$) are used for all the solution domain, and homogeneous grids with the height of $\Delta z = 2$ inches (Case 1), $\Delta z = 4$ inches (Case 2) and $\Delta z = 7$ inches (Case 3) are used respectively for the discretization of the measure domain in longitudinal z direction, and thus we get three results. Afterwards, we use mixed order basis functions instead. That's to say, one order basis functions ($N_u = 1,\ N_v = 1,\ N_w = 1$) are adopted for the non-shadow region and higher order basis functions ($N_u = 1,\ N_v = 1,\ N_w = 2$) for the shadow region, and homogeneous grids with the height of $\Delta z = 7$ inches (Case 4) are used for the discretization of the measure domain in longitudinal z direction. The discretizations are the same in non-measure domain, in both the radial and azimuthal directions of measure domain for Cases 1–4. The number of discretized elements

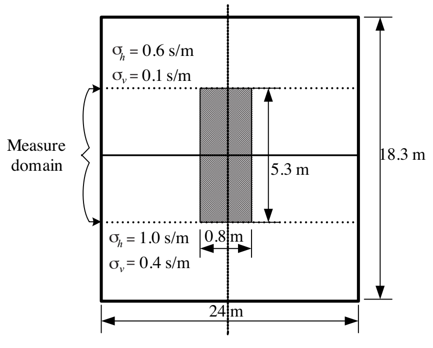

(a) Two-layered formation model

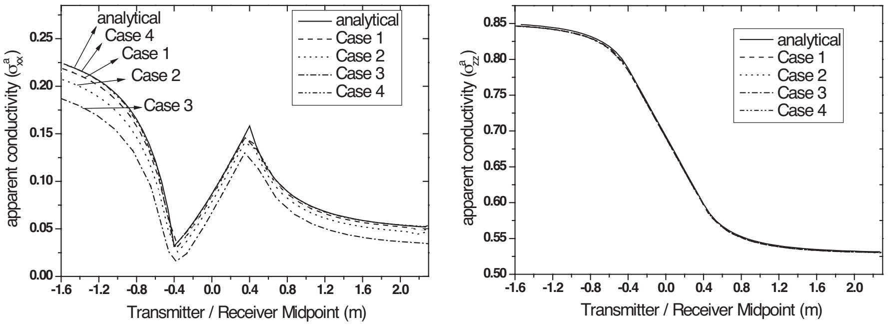

(b) Horizontal apparent conductivity (c) Vertical apparent conductivity

Figure 7. Two-layered formation model and comparison of its responses computed by one order (Cases 1–3) and mix order (Case 4) basis functions.

for the four cases in the radial, azimuthal and longitudinal directions $N_\rho \times N_\varphi \times N_z$ is shown in Table 1. We put together the computation results for Cases 1–4 and analytical result computed by multilayered media Green's functions, as shown in Figs. 7(b) and 7(c). Fig. 7 shows that the apparent vertical conductivity's computational errors, as compared to the analytical result, are quite small for Cases 1–4, while, for Cases 1–3, the computational errors of the horizontal apparent conductivity will become greater and greater as the mesh becomes sparser and sparser. However, the use of mixed order basis functions (Case 4) leads to significant accuracy improvement in the computation of horizontal apparent conductivity. As for the comparisons of the computational cost (grid number, number of unknowns, CPU time of running on SGI-O350 workstation with 1 GHz processors for all measure points) of attaining these results for Cases 1–4, we can find them in Table 1. It is evident that field expansion by mixed order basis functions is significantly more attractive than field expansion by one order basis functions only.

Table 1. Comparisons of computational efforts for Cases 1–4 for the model in Fig. 7(a).

Case	Basis functions	Height (Δz) of mesh in the measure domain (inch)	Number of mesh cells in the measure domain ($N_\rho \times N_\varphi \times N_z$)	Number of mesh cells in the total solution domain ($N_\rho \times N_\varphi \times N_z$)	Total number of unknowns	Time spent in the preprocessing and post-processing on one processor (s)	Time spent in the solution of linear systems by Distributed-SuperLU on six processors (s)
1	One order	2	$21 \times 18 \times 104$	$21 \times 18 \times 128$	149869	795	922
2	One order	4	$21 \times 18 \times 52$	$21 \times 18 \times 76$	88665	454	518
3	One order	7	$21 \times 18 \times 30$	$21 \times 18 \times 54$	62771	335	336
4	Mixed order	7	$21 \times 18 \times 30$	$21 \times 18 \times 54$	77451	384	413

Next, we simulate an eccentric borehole problem, where the tool is not aligned with the borehole axis, as illustrated in Fig. 8(a), and the tool is eccentric toward the x-direction. ρ_e represents the eccentric distance. We investigate the response of the multi-component tool in the model shown in Fig. 8(a) with water-based mud ($\sigma_{mud} = 1\,\mathrm{s/m}$) in a three-layered formation. The upper and lower layers have isotropic conductivity $\sigma_h = \sigma_v = 0.5\,\mathrm{s/m}$, whereas the middle layer has anisotropic conductivity $\sigma_h = 0.2\,\mathrm{s/m}$, $\sigma_v = 0.05\,\mathrm{s/m}$. The middle bed is 3 m thick. The borehole has a radius of 0.1 m. Figs. 8(b), (c), (d) illustrates apparent conductivities σ^a_{xx}, σ^a_{yy} and σ^a_{zz} respectively for three different eccentric distances $\rho_e = 0.0\,\mathrm{m}$, 0.035 m and 0.07 m. The results show that the effect of eccentricity on σ^a_{xx} and σ^a_{zz} is very small, however, its effect on σ^a_{yy} is obvious.

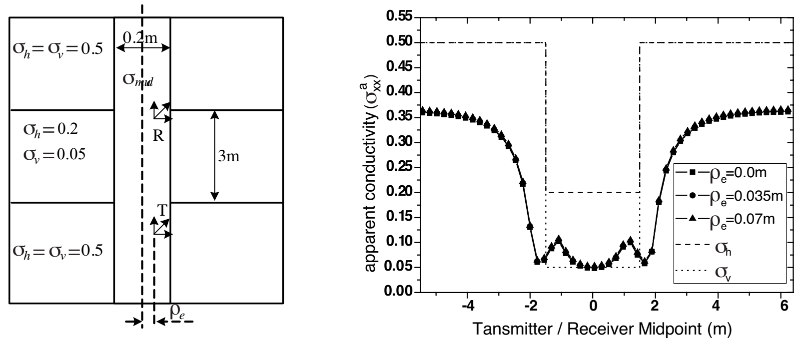

(a) Eccentric tool in three-layered formation with conductive mud

(b) Apparent conductiveities σ^a_{xx}

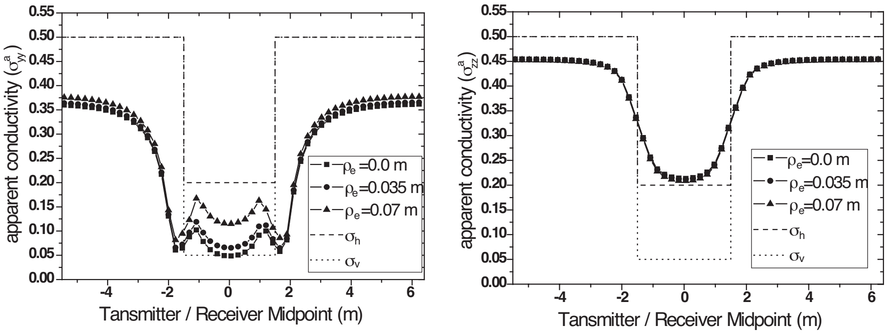

(c) Apparent conductivities σ^a_{yy}

(d) Apparent conductivities σ^a_{zz}

Figure 8. Eccentric tool model and its apparent conductivities from three main components with different eccentric distances.

In addition, nine components of magnetic fields (3 main components: H_{xx}, H_{yy}, H_{zz} and 6 cross-components: H_{yx}, H_{zx}, H_{xy}, H_{zy}, H_{xz}, H_{yz}) computed for the model in Fig. 8(a) with eccentric distances of $\rho_e = 0.0$ and 0.07 m respectively are provided, as shown in Fig. 9. There exists no cross-component when the tool is not eccentric, while there exist cross-components H_{xz} and H_{zx} when the tool is eccentric toward the x direction. What's more, the main-components H_{xx} and H_{yy} won't overlap in the latter case.

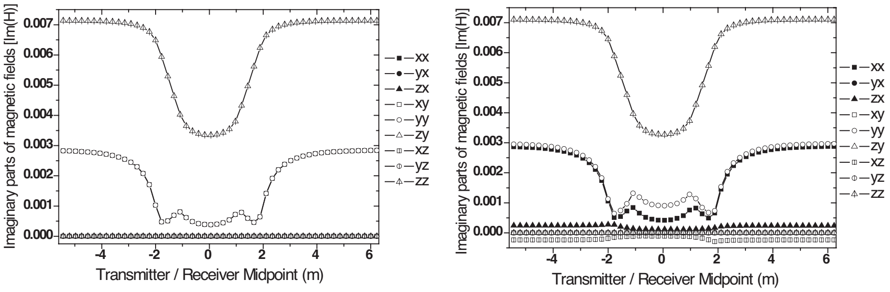

(a) ρ_e=0.0 (b) ρ_e=0.07

Figure 9. Nine components of magnetic fields computed for the model of Fig. 8(a) with eccentric distances $\rho_e = 0.0\,\mathrm{m}$ and $0.07\,\mathrm{m}$ respectively.

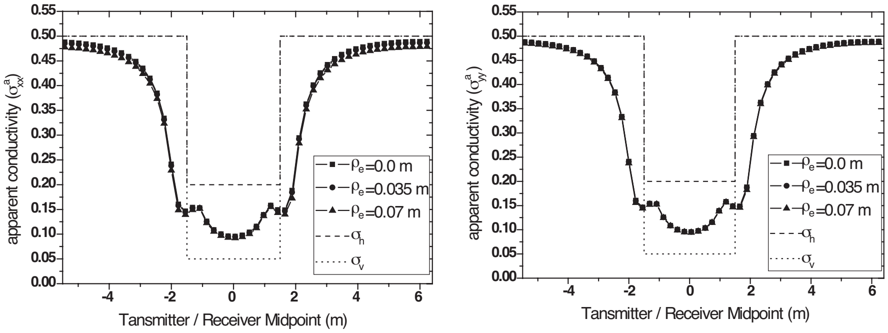

(a) Apparent conductivities σ^a_{xx} (b) Apparent conductivities σ^a_{yy}

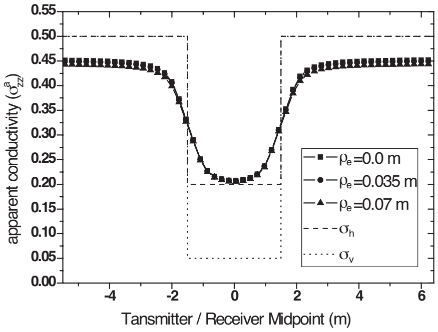

(c) Apparent conductivities σ^a_{xx}

Figure 10. Apparent conductivities from three main components with different eccentric distances (The model parameters are the same as that of Fig. 8(a) with the only change of conductive mud into resistive mud).

Furthermore, we only change water-based mud to oil-based mud ($\sigma = 0.001\,\mathrm{s/m}$), but fix all other parameters in the model of Fig. 8(a) to investigate the tool eccentricity effects in the resistive mud. Fig. 10 shows apparent conductivities σ^a_{xx}, σ^a_{yy} and σ^a_{zz} after the change. From the results, we can see that the effects of eccentricity on apparent horizontal conductivities σ^a_{xx}, σ^a_{yy} and vertical conductivities σ^a_{zz} are very small.

We also compute the response of the tool in dipping bed environments. Model parameters can be seen in Fig. 11(a), and mud conductivity is $1.0\,\mathrm{s/m}$. The formation is dipping towards the x direction. Figs. 11(b), (c), (d) shows respectively the apparent conductivities σ^a_{xx}, σ^a_{yy} and σ^a_{zz} for different dipping angles $\theta = 0°$, $40°$ and $60°$. From the results, We can see that the influence of dipping formation is dramatic on the three apparent conductivities σ^a_{xx}, σ^a_{yy}

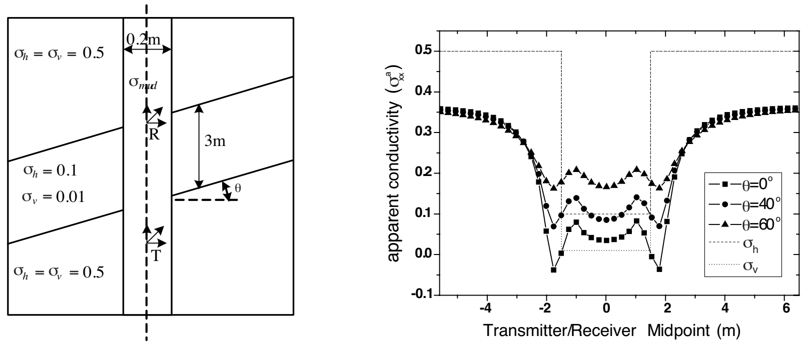

(a) Model of three-layered dipping formation with conductive mud

(b) Apparent conductivities σ^a_{xx}

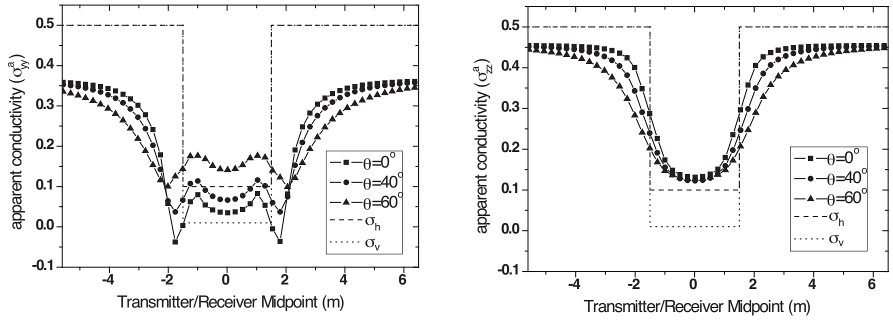

(c) Apparent conductivities σ^a_{yy}

(d) Apparent conductivities σ^a_{zz}

Figure 11. Dipping formation model and apparent conductivities from three main components with different dipping angles.

and σ^a_{zz}, which may mean that it will be more complex to get the true formation parameters from the three apparent conductivities.

In addition, the nine components of magnetic fields computed for the models of Fig. 11(a) with dipping angles of 0° and 60° respectively are also provided, as shown in Fig. 12. The results show very similar behavior to those of eccentricity influence shown in Fig. 9. There exists no cross-component when formations are not dipping, while there exist cross-components H_{xz} and H_{zx} when formations dip toward the x direction. The main-components H_{xx} and H_{yy} won't overlap in the latter case. However, the cross-components produced by dipping formation are generally of bigger values than those produced by eccentric tool.

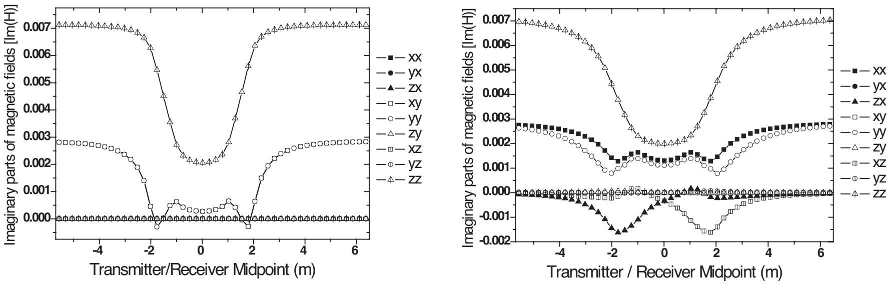

(a) $\theta = 0^\circ$

(b) $\theta = 60^\circ$

Figure 12. Nine components of magnetic fields computed for the models of formations with dipping angles of 0° and 60° respectively in Fig. 11(a).

4. CONCLUSION

We have illustrated the capabilities of a flexible numerical approach based upon the FEM algorithm to study the response of multicomponent induction tool in complex geophysical formations including eccentric borehole and dipping bed. We use conformal cylindrical cells to reduce the staircase error present in the representation of the borehole wall. The use of the mixed order basis functions has proved useful in reducing the number of unknowns and computation time, and the numerical results have demonstrated the validity and efficiency of the scheme. Newly developed package, Distributed-SuperLU, is used for solution of linear equations, and thus multiple measure points can be solved simultaneously.

ACKNOWLEDGMENT

This work was supported by COSL (No. JSB07YF006).

REFERENCES

1. Kriegshauser, B., O. Fanini, S. Forgang, G. Itskovich, M. Rabinovich, L. Tabarovsky, L. Yu, M. Epov, et al., "A new multicomponent induction loggingtool to resolve anisotropic formations," *SPWLA 40th Ann. Log. Symp.*, paper D., 2000.
2. Davydycheva, S., V. Druskinz, and T. Habashyz, "An efficient finite-difference scheme for electromagnetic logging in 3D anisotropic inhomogeneous media," *Geophysics*, Vol. 68, No. 5, 1525–1535, September–October 2003.
3. Wang, T. and S. Fang, "3-D electromagnetic anisotropy modeling using finite differences," *Geophysics*, Vol. 66, No. 6, 1386–1398, 2001.
4. Jin, J. M., *The Finite Element Method in Electromagnetics*, John Wiley & Sons, Inc., New York, 2002.
5. Zhang, Z. Q. and Q. H. Liu, "Applications of the BCGS-FFT method to 3-D induction well logging problem," *IEEE Trans. Geoscience and Remote Sensing*, Vol. 41, 998–1004, May 2003.
6. Ilic, M. M. and B. M. Notaros, "Higher order hierarchical curved hexahedral vector finite elements for electromagnetic modeling," *IEEE Trans. Geosci. Remote Sens.*, Vol. 51, No. 3, 1026–1033, March 2003.
7. Shen, J. S., "Modeling of the 3-D electromagnetic responses to the anisotropic medium by the edge finite element method," *Well Logging Technology of China*, Vol. 28, 11–15, Feb. 2004.
8. Everett, M. E., E. A. Badea, L. C. Shen, G. A. Merchant, and C. J. Weiss, "3-D finite element analysis of induction logging in a dipping formation," *IEEE Trans. Geoscience and Remote Sensing*, Vol. 39, 2244–2252, October 2003.
9. Liu, J. W. H., "The role of elimination trees in sparse factorization," *SIAM J. Matrix Anal. Appl.*, Vol. 11, 134–172, 1990.
10. Demmel, J. W., S. C. Eisenstat, J. R. Gilbert, and X. Y. Li, "A supernodal approach to sparse partial pivoting," *SIAM J. Matrix Anal. Appl.*, Vol. 20, 720–755, 1999.
11. Demmel, J. W., J. R. Gilbert, and X. Y. Li, *SuperLU Users' Guide*, 1999.

12. Zhdanov, M. S., W. D. Kennedy, A. B. Cheryauka, and E. Peksen, "Principles of tensor induction well logging in a deviated well in an anisotropic medium," *SPWLA 42nd Annual Logging Symposium*, June 17–20, 2001.
13. Sun, X. Y., Z. P. Nie, A. Y. Li, and L. Xi, "Numerical modeling of multicomponent induction response in planar layered anisotropic formation," *Chinese Geophysics*, submitted for publication.
14. Avdeev, D. B., A. V. Kuvshinov, O. V. Pankratov, and G. A. Newman, "Three-dimensional induction logging problems, Part 1: An integral equation solution and model comparisons," *Geophysics*, Vol. 67, No. 2, 413–426, March 2002.
15. Zhdanov, M. S., D. Kennedy, and E. Peksen, "Foundation of the tensor induction well logging," *Perophysics*, Vol. 42, No. 6, 588–610, 2001.
16. Riddolls, R. J., "Near-field response in lossy media with exponential conductivity inhomogeneity," *Journal of Electromagnetic Waves and Applications*, Vol. 20, No. 11, 1551–1558, 2006.
17. Golestani-Rad, L. and J. Rashed-Mohassel, "Rigorous analysis of EM-wave penetration into a typical room using FDTD method: The transfer function concept," *Journal of Electromagnetic Waves and Applications*, Vol. 20, No. 7, 913–926, 2006.
18. Chen, X., D. Liang, and K. Huang, "Microwave imaging 3-D buried objects using parallel genetic algorithm combined with FDTD technique," *Journal of Electromagnetic Waves and Applications*, Vol. 20, No. 13, 1761–1774, 2006.
19. Uduwawala, D., "Modeling and investigation of planar parabolic dipoles for GPR applications: A comparison with bow-tie using FDTD," *Journal of Electromagnetic Waves and Applications*, Vol. 20, No. 2, 227–236, 2006.
20. Ding, W., Y. Zhang, P. Y. Zhu, and C. H. Liang, "Study on electromagnetic problems involving combinations of arbitrarily oriented thin-wire antennas and inhomogeneous dielectric objects with a hybrid MOM-FDTD method," *Journal of Electromagnetic Waves and Applications*, Vol. 20, No. 11, 1519–1533, 2006.
21. Zainud-Deen, S. H., W. M. Hassen, E. M. Ali, K. H. Awadalla, and H. A. Sharshar, "Breast cancer detection using a hybrid finite difference frequency domain and particle swarm optimization techniques," *Progress In Electromagnetics Research B*, Vol. 3, 35–46, 2008.

22. Liu, Q. H., "Electromagnetic field generated by an off-axis source in a cylindrically layered medium with an arbitrary number of horizontal discontinuities," *Geophysics*, Vol. 58, No. 50, 616–625, 1993.
23. Pingenot, J., "Full wave analysis of signal attenuation in a lossy rough surface cave using a high order time domain vector finite element method," *Journal of Electromagnetic Waves and Applications*, Vol. 20, No. 12, 1695–1705, 2006.
24. Hernandez-Lopez, M. A. and M. Quintillan-Gonzalez, "A finite element method code to analyse waveguide dispersion," *Journal of Electromagnetic Waves and Applications*, Vol. 21, No. 3, 397–408, 2007.
25. Hatamzadeh-Varmazyar, S., "An integral equation modeling of electromagnetic scattering from the surfaces of arbitrary resistance distribution," *Progress In Electromagnetics Research B*, Vol. 3, 157–172, 2008.
26. Jiang, G. X., H. B. Zhu, and W. Cao, "Implicit solution to modified form of time domain integral equation," *Journal of Electromagnetic Waves and Applications*, Vol. 21, No. 5, 697–707, 2007.
27. Wu, C. G. and G. X. Jiang, "Stabilization procedure for the time-domain integral equation," *Journal of Electromagnetic Waves and Applications*, Vol. 21, No. 11, 1507–1512, 2007.
28. Franceschini, G., "A comparative assessment among iterative linear solvers dealing with electromagnetic integral equations in 3D inhomogeneous anisotropic media," *Journal of Electromagnetic Waves and Applications*, Vol. 21, No. 7, 899–914, 2007.